

# Shape2.5D: A Dataset of Texture-less Surfaces for Depth and Normals Estimation

Muhammad Saif Ullah Khan

Muhammad Zeshan Afzal

Didier Stricker

German Research Center for Artificial Intelligence (DFKI)  
Kaiserslautern, Germany

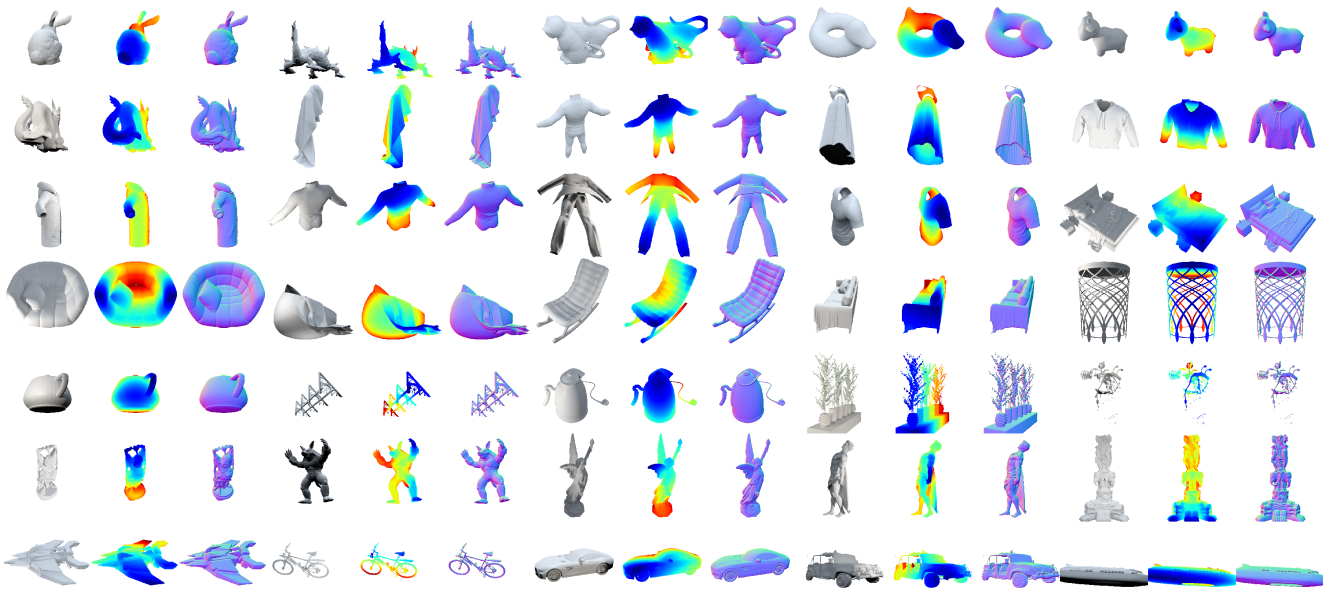


Figure 1. **The Shape2.5D dataset** provides images, depth maps, and normal maps of 2635 3D models comprising 48 unique objects. This includes 13 ShapeNet [6] and 35 other common objects from categories like animals, clothing, furniture, statues, vehicles, and other miscellaneous objects.

## Abstract

Reconstructing texture-less surfaces poses unique challenges in computer vision, primarily due to the lack of specialized datasets that cater to the nuanced needs of depth and normals estimation in the absence of textural information. We introduce "Shape2.5D," a novel, large-scale dataset designed to address this gap. Comprising 364k frames spanning 2635 3D models and 48 unique objects, our dataset provides depth and surface normal maps for texture-less object reconstruction. The proposed dataset includes synthetic images rendered with 3D modeling software to simulate various lighting conditions and viewing angles. It also includes a real-world subset comprising 4672 frames captured with a depth camera. Our comprehensive

benchmarks, performed using a modified encoder-decoder network, showcase the dataset's capability to support the development of algorithms that robustly estimate depth and normals from RGB images. Our open-source data generation pipeline allows the dataset to be extended and adapted for future research. The dataset is publicly available at <https://github.com/saifkhichi96/Shape25D>.

## 1. Introduction

Significant advances have been made in 3D surface reconstruction in recent years [3, 15, 22, 28, 34, 35]. Traditional works [1, 8, 12, 16, 21, 26, 37, 46] have also explored the reconstruction of weakly-textured surfaces. Such surfaces lack distinctive visual cues, which makes it harder to predict

their geometry from an image. However, these surfaces have received limited attention in deep learning [3, 15, 34, 48]. From industrial components [17] and planar surfaces in indoor scenes [16, 21, 48], to biological tissues in medical imaging [5, 12, 40], texture-less surfaces are everywhere. Therefore, the need for effective reconstruction methods is critical and practical.

Deep learning methods rely heavily on data, making it a core foundation of their effectiveness [30]. However, very few shape datasets target texture-less objects [3, 17]. None of these are large-scale like their textured counterparts [6, 31, 43]. Additionally, the available texture-less datasets often only contain partial shape information as depth maps or surface normal maps. Full 3D ground truth in the form of point clouds, meshes, or voxel grids is required to train robust models. The scarcity of extensive, publicly available datasets for low-texture surfaces significantly impedes progress in this field [18]. This makes curating a comprehensive shape dataset of texture-less surfaces paramount. In light of these challenges, we contribute three main items in this work:

- Introducing one of the first synthetic datasets of depth and normal maps of texture-less surfaces containing 48 unique objects rendered from 2635 3D models (Fig. 1).
- A supplementary dataset of six real-world texture-less objects containing 4,345 samples captured with a depth camera.
- A comprehensive benchmark demonstrating the effectiveness of our dataset in reconstructing depth and surface normal maps from RGB images.
- Open-sourced data generation and collection pipelines, enabling researchers to extend the dataset.

By addressing the data scarcity issue head-on, we aim to pave the way for future research in texture-less surface reconstruction.

## 2. Related Work

**Depth and Normals Estimation** Depth estimation [11, 13, 14, 24, 29] determines the distance of each point in the image from the camera. On the other hand, surface normals estimation [19, 20, 36] identifies the direction a surface faces at each point, which is vital for understanding the shape and contours of objects within the image. When used together, these measurements are sometimes referred to as a 2.5D representation in literature [41]. This approach provides a partial but informative view of the spatial relationships in a scene and serves as an intermediary step toward full 3D reconstruction.

**3D Reconstruction** 3D reconstruction involves converting 2D image data into 3D models through various techniques [2, 7, 9, 18, 23, 25, 32, 33, 35, 39, 44, 45, 47, 50, 51]. There are several ways of reconstructing an object in 3D. Some methods use point clouds [15, 28] to identify key points in

space and recreate the object’s surface. Other methods use voxels to represent the 3D volume in a grid [9, 22, 27, 33, 42–45]. Additionally, some approaches reconstruct meshes that use vertices and interconnected faces to create a highly detailed representation of the object [32, 35, 49].

**Texture-less Surfaces** Traditional vision-based works have attempted to reconstruct texture-less surfaces using different methods. [8, 26] project pattern onto the surface, [16] uses a multi-camera setup to establish correspondences between pixels in different views of the surface, and [12] combines stereovision with Shape from Shading. [3, 34] pioneered the texture-less object reconstruction in deep learning. [3] also published a dataset of textureless clothes, which was used by some later works [15, 34].

**Datasets for Surface Reconstruction** Datasets like ShapeNet [6], Pix3D [31], and Things3D [43] have significantly contributed to the progress in textured object reconstruction. Their extensive samples and variety have established benchmarks in the domain. However, texture-less objects have not received a similar focus, with datasets such as T-LESS [17] and the work by [3] offering limited diversity. Our dataset addresses this imbalance, providing a broader collection of texture-less surfaces, accompanied by detailed depth and normal maps, to foster advancements in shape reconstruction from texture-less data.

## 3. The Shape2.5D Dataset

In this section, we explain our dataset and its creation process. The dataset has a synthetic component rendered in Blender [10] and a real-world component obtained from a Microsoft Kinect V2 camera. These are discussed in Sec. 3.1 and 3.2, respectively.

### 3.1. Synthetic Data

The synthetic dataset is divided into two logical subsets. The first set consists of 35 everyday objects organized into six broader categories, namely *animals*, *clothing*, *furniture*, *statues*, *vehicles*, and *miscellaneous*. Each object in this subset has one 3D model, shown in Fig. 1. Clothing and furniture items are commonly found in natural scenes and are often minimally textured or completely texture-less. Architectural sculptures are also a regular feature in many real-world settings worldwide, often without colors or elaborate textures. The dataset includes several statues, including intricate, life-size 3D models with complex shapes and depth variations. We provide images, depth maps, and surface normal maps for each object.

Changes in lighting and shadows are some of the few noticeable visual cues for texture-less objects with otherwise homogeneous surfaces. However, these changes are not enough to indicate their 3D shape. We provide object renders from multiple angles and under different lighting conditions to aid networks in learning illumination-independent

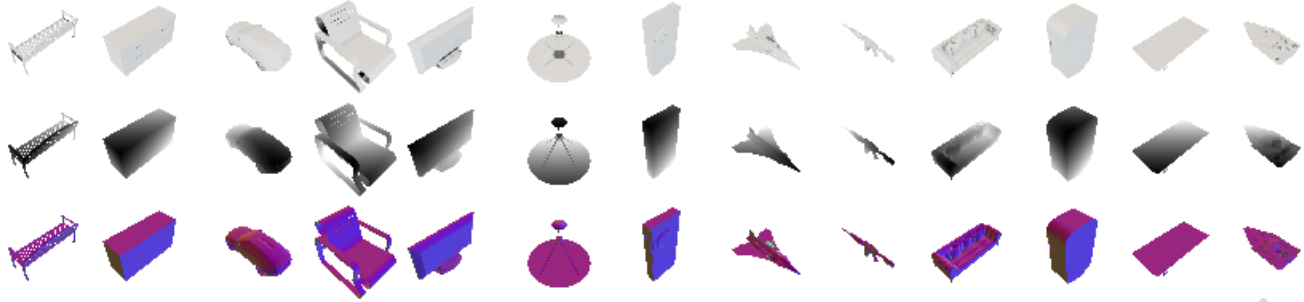


Figure 2. **The ShapeNet category.** 24 renders of 200 models for 13 main ShapeNet objects, depth maps, and surface normals are provided.

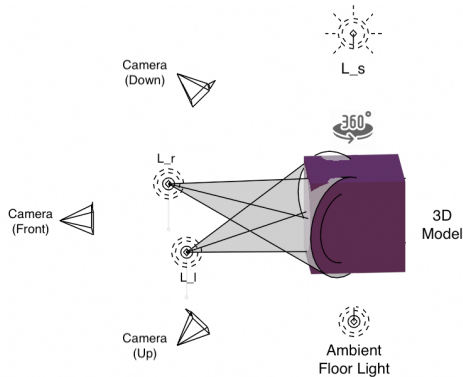


Figure 3. **The Blender scene.** The object is illuminated by several lights and captured by three different cameras while rotating to capture multiple views.

features for object reconstruction. Each object is rendered 8,640 times, with 24 configurations featuring 360 views each. These are described in Sec. 3.1.2.

The second subset of the synthetic dataset also referred to as the *shapenet* category, consists of 13 objects selected from the Choy et al. [9] subset of the ShapeNet dataset [6]. This set focuses on diverse 3D shapes rather than lighting changes to the same 3D model. It includes 200 models for each object, but we only render 24 samples for each model using a constant lighting setup. We still render the objects from all three cameras, but only from eight views instead of 360. Fig. 2 shows some rendered samples from this subset.

### 3.1.1 Scene Setup

Imitating the scene setup of [3], we created a Blender scene with multiple lights and cameras around the object. The setup is illustrated in Fig. 3. Each camera looks at the object from a different perspective, and several lights ensure the object is adequately illuminated with realistic shadows.

There are three cameras in the scene. The first camera is positioned parallel to the object in front, while the other two are placed at slightly elevated angles above and below the

	Sequence	Description
<b>Lights</b>	$L_s$	Only sunlight on.
	$L_l$	Left lamp and sunlight on.
	$L_r$	Right lamp and sunlight on.
	$L_a$	Both lamps and sunlight on.
<b>Camera</b>	down	Above the object, looking down.
	front	At object height, looking straight.
	up	Below the object, looking up.
<b>Color</b>	Yes	Uniform color on the model.
	No	Model completely colorless.

Table 1. **Rendering Configurations.** We use different combinations of lights, cameras, and colors to generate sequences of data.

object. The front camera remains stationary, but the exact tilt angle of the other two cameras is randomly changed to ensure a variety of elevations. Additionally, the object is rotated by small azimuth steps around itself, providing comprehensive coverage from all sides.

Like natural scenes, which have multiple light sources affecting how a surface is perceived, we include various lights to simulate realistic shadows and illuminations. Two bright spotlights shine on the object from the front-left and front-right sides. These lights have a warm white color resembling the standard incandescent lamps with an RGB value of (1.0, 0.945, 0.875). A blue-tinted cool sunlight with RGB value (0.785, 0.883, 1.0) is added overhead, and a soft glowing white ambient light is placed on the floor to light up the bottom faces of the object. The sunlight has a power of 100 watts per square meter, while the ambient floor light has a power of 2 watts per square meter. The brightness of the spotlights varies based on the object’s distance from the cameras.

### 3.1.2 Configurations

The scene is rendered under different lighting configurations, with one or more lights on at a time. This generates a

Category	Objects	Configurations				Splits		
		Models	Sequences	Views	Samples	Train	Val	Test
animals	asian_dragon, cats, duck, pig, stanford_bunny, stanford_dragon	6	24	360	51,840	$Ll_{down}, Ll_{front}, Ll_{up}, Lr_{down}, Lr_{front}, Lr_{up}, Ls_{down}, Ls_{front}$	$La_{down}, La_{front}$	$La_{up}, Ls_{up}$
clothing	cape, dress, hoodie, jacket, shirt, suit, tracksuit, tshirt	8	24	360	69,120	$Lr_{front}, Lr_{up}, Ls_{down}, Ls_{front}$		
furniture	armchair, bed, chair, desk, rocking_chair, sofa	6	24	360	51,840			
statues	armadillo, buddha, lucy, roman, thai	5	24	360	43,200			
vehicles	bicycle, car, jeep, ship, spacehip	5	24	360	43,200			
misc	diego, kettle, plants, teapot, skeleton	5	24	360	43,200			
shapenet	plane, bench, cabinet, car, chair, display, lamp, speaker, rifle, sofa, table, phone, watercraft	2600	24	360	62,400	$La_{down}, La_{up}, La_{front} (0^\circ, 45^\circ, 90^\circ, 180^\circ, 225^\circ, 270^\circ)$	$La_{down}, La_{up}, La_{front} (135^\circ)$	$La_{down}, La_{up}, La_{front} (315^\circ)$

Table 2. **Shape2.5D-Synthetic**. This subset contains 48 objects with 2635 unique 3D models and 364,800 samples in total.

wide range of shadows and lighting effects in the dataset. It can help deep learning networks comprehend the impact of shadows on shape perception, resulting in networks that are robust to lighting variations.

We note that texture-less surfaces do not necessarily lack color. Rather, they lack distinctive textures on their surfaces. We expand the definition of texture-less surfaces to include any surfaces with a uniform color. As a result, we render all objects once without color or texture and again with a diffuse material of a random but uniform color applied to the entire surface. This is different from [3], where all objects are only grayscale.

Using the cameras, lighting, and colors described above, we have 24 different configurations. These are summarized in Tab. 1. Each 3D model is rendered from different rotation angles under all these configurations, as described in the next section.

### 3.1.3 Rendering Pipeline

We use an automated script to generate data with Blender. The script creates a 3D scene with the required settings, including camera and lighting. It then enables rendering passes to capture RGB images and depth maps and sets up compositor nodes within Blender for post-processing rendered data. The 3D models are imported from Wavefront files located in the specified path. After importing, they are positioned at the origin with the appropriate scale and orientation, ensuring they are visible and upright within the camera viewport. All textures are removed, leaving only the bare 3D model.

We select one model at a time and rotate it through specified steps to render a sequence of views. This process is

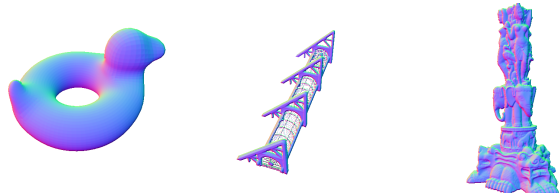


Figure 4. **Depth Complexity**: A simple rubber duck, the detailed San Diego Convention Center, and an intricate Thai statue.

repeated for each enabled camera and lighting setup. For each view, an RGB image, a foreground mask, and a depth map are rendered. The rendered images have a resolution of 512x512 and a black background. Following [3], surface normals are computed by differentiating the depth maps.

**Depth Complexity.** Our dataset comprises objects with varying shapes and degrees of realism regarding deformations and size variations. These objects range from a tiny rubber duck to several life-size statues and a model of the San Diego Convention Center building (as shown in Fig. 4).

**Rendering Environment** We used Cycles, a ray-tracing engine, to render images on an Intel(R) Core(TM) i7-6700K CPU with a 4.00GHz processor. Each sample took around 30 seconds to generate. This time reduces to 5 seconds if a GPU rendering with CUDA is used. Our rendering script also supports the physically-based Eevee renderer.

### 3.1.4 Data Splits

Tab. 2 outlines the configuration of the synthetic dataset and the designated data splits. The dataset encompasses 48 objects across seven subcategories, with 2635 unique 3D models contributing to 364,800 samples. The dataset is

partitioned into training, validation, and testing subsets for each category. The splits for the primary six categories are crafted to support inter-category and intra-category evaluation scenarios. In inter-category experiments, models are trained on one category and then assessed on the others to examine the network’s ability to generalize across different shape categories and objects. Intra-category experiments, conversely, involve training and testing within the same category to evaluate the network’s generalization to new lighting conditions for previously encountered views.

### 3.2. Real-World Dataset

To supplement the synthetic texture-less data, we also collected a small dataset of real-world low-texture objects containing 4,672 samples from six objects. This includes four deformable objects *hoody*, *shirt*, *shorts*, and *tshirt*, and two rigid objects *chair* and *lamp*. Unlike the dataset used by [3], which relied on controlled artificial lighting, we collected our data under natural daylight as well as multiple random artificial light sources. We explain the collection process in the following section. Tab. 3 provides a summary of the objects in our real-world dataset.

#### 3.2.1 Collection Process

We recreated the setup depicted in Fig. 3 in a real-world environment. The Kinect was mounted on a tripod with adjustable height, facing away from a large window that allowed natural light into the room. The room was illuminated by a combination of natural light from the window and four different fluorescent light bulbs. The objects were placed at distances ranging from 0.5m to 1.25m from the camera. As the accuracy of depth values obtained through Kinect can be affected by temperature [38], we allowed the camera to run for 30 minutes to reach a stable temperature before starting data capture each time. We varied the camera height and viewing angle to obtain the *up*, *down*, and *front* camera positions. The light bulbs were switched on and off randomly to provide different lighting across sequences. Each sequence had at least two lights to create complex shadows.

For data collection, the clothing pieces were worn by an individual who moved randomly in front of a camera. Meanwhile, other objects were positioned on a stationary surface and manually rotated in front of the camera. The camera captured synchronized RGB images and depth maps. In the post-processing stage, described in the next section, a segmentation algorithm selected only the object of interest and removed the person and any background. The surface normals were then computed by smoothing the depth maps using a  $5 \times 5$  Gaussian filter and differentiating them.



Figure 5. The top row of the figure shows the results of our skin-detection algorithm that removes the person wearing the clothes from the images. The middle row shows the raw output from Kinect with a lot of noise and a hole in the depth and normal maps (right leg). The bottom row shows the output after post-processing.

Object	hoody	shirt	shorts	tshirt	chair	lamp
Sequences	3	4	1	9	2	1
Samples	508	671	387	1545	1201	360

Table 3. Summary of objects in the dataset of real objects.

#### 3.2.2 Post-Processing

After capturing raw data with the Kinect camera, we perform several post-processing steps to prepare it for use. These steps are summarized in Fig. 5.

**Hole filling.** The Kinect uses phase-shifted infrared light to compute depth, but it can sometimes miss surfaces that absorb infrared waves, are translucent, or very shiny. This results in holes in the depth map. To fix this, we used OpenCV’s implementation of the Navier-Stokes-based method [4] of inpainting with a radius of 7, which interpolates the missing parts.

**Background segmentation.** To identify the body of a person wearing clothes, a naive skin-color detection algorithm initialized with an estimated skin color of the person was used. For objects placed on a flat surface, the surface was covered with a skin-colored cloth. In the captured image, any skin-colored pixels or those more than 1.25 meters away from the camera were considered background. We removed the background and filtered out small contours as noise that escaped skin detection. The largest contour in the scene was identified as the foreground, which contained the object of interest. Finally, we performed a morphological closing operation to fill any small holes in the foreground mask. We have included a binary mask of the foreground for each sample in the dataset.

**Normalization.** The normal vectors were transformed into unit-length vectors with values ranging from -1 to 1. This was achieved by dividing each vector by its magnitude. Additionally, all depth values in the dataset were normalized between 0 and 1. This was done to ensure that the dataset remains invariant to the arbitrary choice of camera distance from the object. The background pixels were assigned a depth value of 1 while the foreground pixels had values ranging between 0 and 0.99.

## 4. Experiments

To showcase the usability of our dataset, we evaluated it on a pre-existing neural network to estimate the depth and surface normals of texture-less objects.

### 4.1. Baseline

Bednarik et al. [3] showed that their encoder-decoder network is a good starting point for reconstructing depth and normal maps from a single image of deformable, texture-less surfaces. It is the closest work to our task, for which we created a new dataset. Inspired by their results, we used their network as a baseline for our benchmarks by removing the mesh decoder. However, unlike [3], we trained the depth and normal decoders jointly without using early stopping. We kept all other hyper-parameters the same and added an edge consistency component to the original depth and normal loss functions of [3] by computing the MSE loss for the gradients of the depth and normal maps. In all experiments, we trained the network for 50 epochs.

### 4.2. Evaluation Metrics

The depth error metric, denoted as  $E_D$ , measures the absolute difference between the predicted and actual depth values, considering only the foreground pixels. Since the depth values are normalized between 0 and 1, the metric does not represent real-world units but rather a percentage. We represent the mean absolute difference in depth values as a percentage multiplied by 100.

The normals error metric, denoted as  $E_N$ , is the mean angular distance in degrees between the surface normals of the predicted and actual values. Smaller values of  $E_D$  and  $E_N$  indicate better results. Additionally, we report the percentage of surface normals with errors of less than  $10^\circ$ ,  $20^\circ$ , and  $30^\circ$ , respectively. Higher percentages indicate better quality of normal vectors. It is important to note that only foreground pixels are used to calculate all metrics, as background pixels are not labeled.

### 4.3. Benchmarks

#### 4.3.1 Intra-Category Benchmark

Tab. 4 shows the performance of the baseline network trained on objects in each of the six main categories and evaluated

on a subset of the same objects in unseen lighting conditions. The results demonstrate that the network successfully learns the shape of the texture-less objects under illumination changes reasonably well.

Dataset	$E_D$	$E_N$	$<10^\circ$	$<20^\circ$	$<30^\circ$
<b>animals</b>	5.02± 5.02	14.19±10.75	63.83	81.84	88.56
<b>clothing</b>	2.61± 1.66	10.59± 2.64	67.69	87.47	93.88
<b>furniture</b>	3.79± 5.73	11.67± 8.13	69.33	84.82	91.17
<b>misc</b>	2.99± 1.71	16.98±10.25	58.25	73.38	81.63
<b>statues</b>	5.83± 7.06	16.58±10.02	50.76	75.31	86.00
<b>vehicles</b>	4.08± 5.60	16.31± 8.61	55.41	73.88	83.62

Table 4. **Intra-Category Benchmark.** The clothing and furniture categories show the best results with more than 93.88% and 91.17% of the predicted normals, respectively, having smaller than  $30^\circ$  angular difference from the groundtruth. This shows that our dataset allows for a good inter-class generalization ability.

#### 4.3.2 Inter-Category Benchmarks

Objects in a single category sometimes share similar geometric structures. For example, all the statues have humanoid shapes with faces, torsos, arms, and legs, and many small but gradual surface orientation changes. On the other hand, the furniture primarily consists of plain surfaces with sharp corners and planes, often bending at right angles. Tab. 5 lists the results of the inter-category experiments with networks trained on one object category and evaluated on objects in all other categories. These experiments show the ability of the network to learn geometry-independent features and generalize to new types of texture-less objects.

Fig. 7 visualizes the network output trained on the synthetic furniture category on three randomly selected furniture objects and a statue, showing the strongest errors near the edges.

#### 4.3.3 ShapeNet Benchmark

For the shapenet category, Tab. 6 shows the results for each object. During training, the network viewed each of the 200 3D models for all 13 objects from six of the eight azimuth angles. Results were evaluated on one previously unseen view of all 3D models and reported individually for each object. These results are significantly better than the main categories because of a much higher number of 3D models.

#### 4.3.4 Real-World Benchmarks

We evaluated the baseline network trained on the 'clothing' subset of our synthetic dataset on this real-world data and report the results in Tab. 7. The complete real dataset is used as the test set. Fig. 6 shows the qualitative results of these experiments on a random sample from the dataset.

Train	Test	$E_D$	$E_N$	$<10^\circ$	$<20^\circ$	$<30^\circ$
animals	clothing	20.76±6.34	26.71±7.79	15.93	50.65	72.43
	furniture	21.28±6.91	<b>26.09±8.99</b>	<b>22.58</b>	<b>53.13</b>	<b>73.27</b>
	misc	<b>20.72±9.07</b>	43.63±19.47	14.37	36.85	51.56
	statues	26.37±7.16	41.37±14.86	11.55	36.26	56.71
	vehicles	20.83±4.69	53.61±24.12	9.48	27.09	41.98
clothing	animals	<b>19.35±4.78</b>	<b>25.18±4.31</b>	<b>18.13</b>	<b>52.36</b>	<b>72.06</b>
	furniture	20.50±4.54	29.28±7.18	13.65	39.79	64.97
	misc	20.61±6.16	39.39±10.05	11.43	30.97	48.97
	statues	19.85±5.43	29.08±6.70	17.48	44.56	64.9
vehicles	animals	<b>22.40±6.02</b>	<b>31.14±7.47</b>	<b>14.04</b>	<b>40.22</b>	<b>61.73</b>
	clothing	24.84±5.29	35.53±8.82	8.92	30.96	54.44
	misc	23.07±8.65	43.79±14.35	10.75	29.13	45.83
	statues	29.57±8.29	41.20±11.80	8.42	28.00	49.57
misc	animals	21.55±5.54	38.49±7.42	11.24	31.85	50.48
	clothing	25.76±5.89	35.46±6.01	8.36	30.40	52.85
	furniture	23.36±5.73	36.95±8.57	14.38	35.58	53.89
	statues	<b>19.77±6.41</b>	<b>33.85±9.95</b>	<b>18.80</b>	<b>38.04</b>	<b>54.93</b>
statues	vehicles	21.15±6.82	48.60±14.74	8.47	24.17	39.58
	animals	<b>20.85±5.15</b>	<b>38.34±7.54</b>	<b>12.14</b>	<b>35.67</b>	<b>55.39</b>
	clothing	22.66±5.14	40.87±9.28	7.93	28.52	51.64
	furniture	23.78±5.21	48.09±11.43	9.72	30.26	47.85
vehicles	misc	22.70±6.07	49.31±10.18	8.62	25.32	40.49
	animals	23.85±5.48	50.93±12.51	7.37	23.95	40.36
	clothing	23.24±6.67	<b>29.28±4.95</b>	15.57	<b>44.04</b>	<b>65.01</b>
	statues	23.29±7.87	32.59±6.79	15.90	40.90	59.69
vehicles	furniture	<b>22.08±5.87</b>	32.92±6.58	<b>16.21</b>	41.33	60.14
	misc	23.90±7.17	41.13±12.24	13.61	34.77	49.95
	statues	29.83±9.69	31.36±6.63	13.80	39.77	61.51

Table 5. **Inter-Category Benchmark.** The degree of generalization to new categories is less than that for objects within the same category ( Tab. 4). The network learns strong shape priors that do not generalize well to very different geometries.

Object	$E_D$	$E_N$	$<10^\circ$	$<20^\circ$	$<30^\circ$
plane	17.59±7.73	35.35±19.50	24.56	41.64	52.46
bench	13.05±4.63	25.60±9.13	34.73	53.43	65.27
cabinet	<b>8.23±4.01</b>	<b>12.60±6.26</b>	<b>76.97</b>	<b>85.01</b>	<b>87.89</b>
car	8.26±3.84	22.14±9.87	39.91	62.05	74.28
chair	14.75±5.36	24.08±13.37	39.51	59.29	70.58
display	13.13±6.07	22.53±12.51	50.91	67.26	75.14
lamp	16.71±9.59	26.48±9.97	25.13	47.56	64.55
speaker	9.76±5.61	16.03±10.90	63.61	76.50	83.26
rifle	17.71±7.94	33.97±16.57	21.60	40.50	53.67
sofa	9.25±3.57	14.00±6.71	62.51	78.66	86.25
table	12.02±4.78	18.99±13.59	57.85	68.77	75.78
phone	13.90±8.78	24.55±14.17	50.08	66.60	74.90
watercraft	15.24±8.13	28.06±15.60	32.85	50.63	62.63

Table 6. **ShapeNet Benchmark.** Performance improves greatly when more shapes are seen during training. This shows the network can learn shape representations from our texture-less renders.

To further demonstrate the generalization capability of the network to real-world data, we choose the real texture-less dataset from Bednarik et al. [3]. This dataset has five

Object	$E_D$	$E_N$	$<10^\circ$	$<20^\circ$	$<30^\circ$
chair	29.62±8.89	43.68±8.54	10.15	31.39	49.84
hoodie	36.60±8.54	36.55±3.68	9.38	31.37	55.20
lamp	23.30±6.27	74.26±7.07	3.39	11.85	21.88
shirt	36.99±7.85	36.24±4.41	8.88	31.54	56.49
shorts	42.35±7.12	26.78±3.01	12.68	42.35	73.03
tshirt	36.12±9.22	35.45±3.38	10.20	34.77	59.92

Table 7. **Shape2.5D-Real Benchmark.** Results of reconstructing depth and normal vectors of our real dataset using the baseline network trained on our synthetic clothing dataset.



Figure 6. **Qualitative Results of Shape2.5D-Real Benchmark.** Visualization of the qualitative errors on a random sample from our real-world test data.

items, and [3] defines an experiment where the *cloth* object is used to train the network, and 100 samples from each object are used for testing. Using the configuration defined in Sec. 4.1, we train the network on the real images of *cloth* object from [3]. In Tab. 8, this network’s performance for the surface normals map reconstruction task is compared with the network trained on the synthetic clothing category. Results for the shapenet category are provided in the supplemental material, where results of experiments on another real-world dataset that we created are also reported.

## 5. Beyond Shape2.5D

Our dataset generation and collection process is completely automated and can be reproduced easily. We will make the source code publicly available, which can be used to generate more data samples. The input requires Wavefront files that support a flat folder structure or a ShapeNet-like hierarchy. Users can generate datasets with Blender-exported surface normals or computed normals from depth maps. See the datasheet in Appendix A for comprehensive documentation. Appendix B provides data sources, access information, and license details.

## 6. Conclusion

This work introduces the first extensive depth and surface normals dataset dedicated to texture-less surfaces, marking

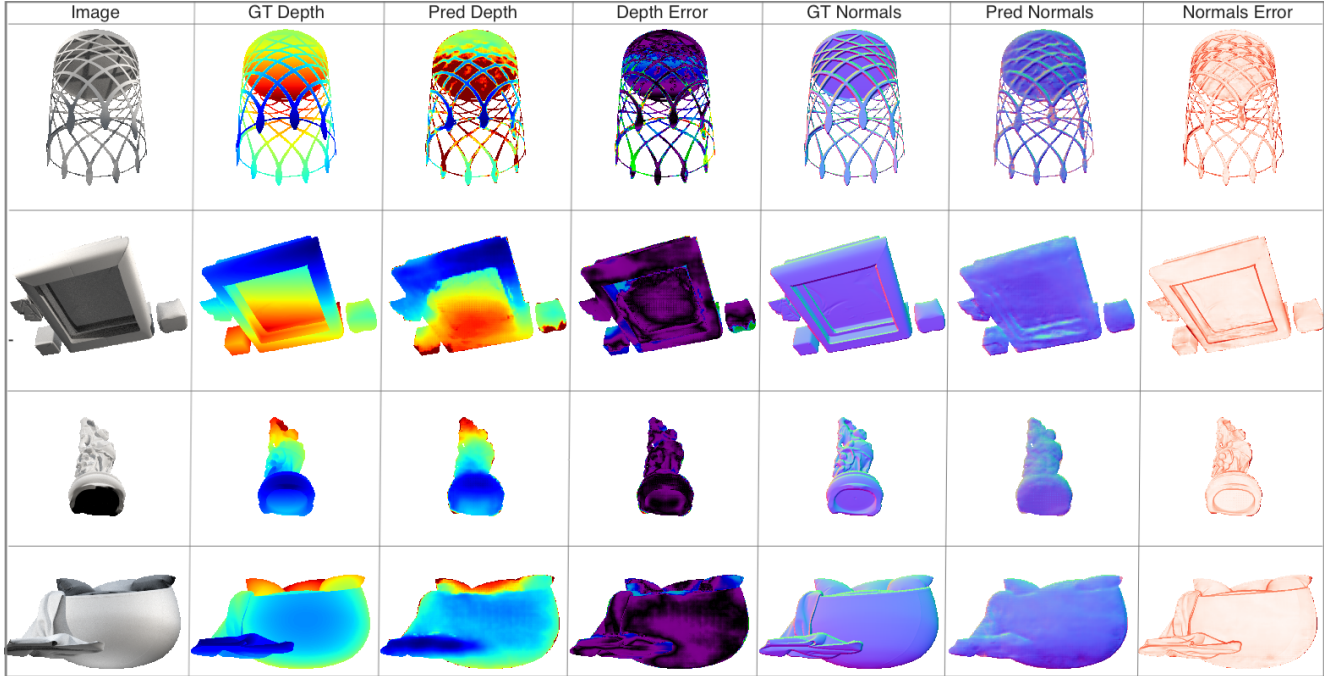


Figure 7. **Qualitative Results of Synthetic Benchmarks.** Visualization of the qualitative errors on random samples in the test data.

Test	Train	$E_N$	$<10^\circ$	$<20^\circ$	$<30^\circ$
cloth	S	$37.58 \pm 5.95$	6.46	22.46	42.92
	R	<b><math>33.96 \pm 6.47</math></b>	<b>11.31</b>	<b>32.95</b>	<b>53.40</b>
hoody	S	<b><math>36.96 \pm 2.31</math></b>	<b>6.58</b>	<b>23.95</b>	<b>45.74</b>
	R	$40.94 \pm 2.85$	5.29	18.95	36.70
paper	S	<b><math>43.87 \pm 6.92</math></b>	<b>4.28</b>	<b>16.08</b>	<b>32.24</b>
	R	$45.91 \pm 7.32$	4.02	15.19	30.54
sweater	S	<b><math>40.66 \pm 2.66</math></b>	<b>4.73</b>	<b>17.90</b>	<b>36.51</b>
	R	$47.85 \pm 3.67$	3.26	12.60	26.45
tshirt	S	<b><math>35.89 \pm 4.27</math></b>	<b>6.85</b>	<b>24.68</b>	<b>46.71</b>
	R	$42.43 \pm 6.24$	4.56	17.15	34.34

Table 8. **Bednarik-Real Benchmark.** Comparison of normal map reconstruction between a network trained on our synthetic dataset (S) and the same network trained on real *cloth* data from [3] (R). When trained on our synthetic data, the same network gives better surface normals for all four real objects other than the *cloth* object used to train the real network, where our results are comparable.

a significant step forward in 3D shape analysis. The dataset contains depth and surface normal maps, providing a 2.5D representation of object shapes. While this offers only a partial geometry from a single viewpoint, it sets a foundation for reconstructing texture-less surfaces—a nascent but growing area of research.

The choice of synthetic data over real-world data addresses the complexity of large-scale 3D data acquisition. We align our normal maps computation with existing method-

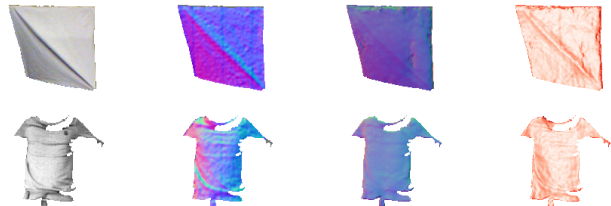


Figure 8. **Qualitative Results of Bednarik-Real Benchmark.** Visualization of the output on real objects from [3] when trained on our synthetic data.

ologies for consistency while offering an avenue for generating more accurate normals using Blender’s capabilities. This flexibility supports future work in synthetic data generation that may require higher fidelity in surface normal representation.

Our dataset surpasses existing ones in size and diversity, offering a new benchmark for texture-less surface reconstruction methods. Future research can leverage this dataset to test the scalability and generalizability of existing approaches. Additionally, providing source code enables the community to expand the dataset further—both in complexity, by introducing scenes with multiple objects and varied backgrounds, and in scope, by incorporating more 3D models from repositories such as ShapeNet.

Exploring the direct reconstruction of voxel representations from our dataset presents another promising research

avenue. Such work could significantly advance shape understanding and reconstruction techniques, particularly for texture-less objects.

**Ethical Considerations** We acknowledge the inclusion of cultural and religious symbols in our 3D models. All images are rendered respectfully, ensuring the depictions remain neutral and free from offensive contexts.

**Acknowledgments** We extend our gratitude to the ShapeNet repository contributors for providing the 3D models that partly form the basis of our dataset and to the Blender developers for the software that enabled our renderings.

## References

- [1] Ali Hosseinaveh Ahmadabadian, Ali Karami, and Rouhollah Yazdan. An automatic 3d reconstruction system for texture-less objects. *Robotics and Autonomous Systems*, 117: 29–39, 2019. [1](#)
- [2] Kalyan Vasudev Alwala, Abhinav Gupta, and Shubham Tulsiani. Pre-train, self-train, distill: A simple recipe for super-sizing 3d reconstruction. In *Proceedings of the IEEE/CVF Conference on Computer Vision and Pattern Recognition*, pages 3773–3782, 2022. [2](#)
- [3] Jan Bednarik, Pascal Fua, and Mathieu Salzmann. Learning to reconstruct texture-less deformable surfaces from a single view. In *2018 International Conference on 3D Vision (3DV)*, pages 606–615. IEEE, 2018. [1](#), [2](#), [3](#), [4](#), [5](#), [6](#), [7](#), [8](#)
- [4] Marcelo Bertalmio, Andrea L Bertozzi, and Guillermo Sapiro. Navier-stokes, fluid dynamics, and image and video inpainting. In *Proceedings of the 2001 IEEE Computer Society Conference on Computer Vision and Pattern Recognition. CVPR 2001*, pages I–I. IEEE, 2001. [5](#)
- [5] Judith Böven, Johannes Boos, Andrea Steuwe, Janna Morawitz, Lino Morris Sawicki, Julian Caspers, Lisa Küppers, Benno Hartung, Christoph Thomas, Gerald Antoch, et al. Diagnostic value and forensic relevance of a novel photorealistic 3d reconstruction technique in post-mortem ct. *The British Journal of Radiology*, 93(1112):20200204, 2020. [2](#)
- [6] Angel X. Chang, Thomas Funkhouser, Leonidas Guibas, Pat Hanrahan, Qixing Huang, Zimo Li, Silvio Savarese, Manolis Savva, Shuran Song, Hao Su, Jianxiong Xiao, Li Yi, and Fisher Yu. Shapenet: An information-rich 3d model repository. Technical Report arXiv:1512.03012 [cs.GR], Stanford University — Princeton University — Toyota Technological Institute at Chicago, 2015. [1](#), [2](#), [3](#)
- [7] Yixin Chen, Junfeng Ni, Nan Jiang, Yaowei Zhang, Yixin Zhu, and Siyuan Huang. Single-view 3d scene reconstruction with high-fidelity shape and texture. *arXiv preprint arXiv:2311.00457*, 2023. [2](#)
- [8] Ziang Cheng, Hongdong Li, Yuta Asano, Yinqiang Zheng, and Imari Sato. Multi-view 3d reconstruction of a texture-less smooth surface of unknown generic reflectance. In *Proceedings of the IEEE/CVF Conference on Computer Vision and Pattern Recognition*, pages 16226–16235, 2021. [1](#), [2](#)
- [9] Christopher B Choy, Danfei Xu, JunYoung Gwak, Kevin Chen, and Silvio Savarese. 3d-r2n2: A unified approach for single and multi-view 3d object reconstruction. In *Proceedings of the European Conference on Computer Vision (ECCV)*, 2016. [2](#), [3](#)
- [10] Blender Online Community. *Blender - a 3D modelling and rendering package*. Blender Foundation, Stichting Blender Foundation, Amsterdam, 2018. [2](#)
- [11] Alex Costanzino, Pierluigi Zama Ramirez, Matteo Poggi, Fabio Tosi, Stefano Mattoccia, and Luigi Di Stefano. Learning depth estimation for transparent and mirror surfaces. In *Proceedings of the IEEE/CVF International Conference on Computer Vision*, pages 9244–9255, 2023. [2](#)
- [12] Jiacheng Fan, Yuan Feng, Jinqiu Mo, Shigang Wang, and Qinghua Liang. 3d reconstruction of non-textured surface by combining shape from shading and stereovision. *Measurement*, 185:110029, 2021. [1](#), [2](#)
- [13] Stefano Gasperini, Nils Morbitzer, HyunJun Jung, Nassir Navab, and Federico Tombari. Robust monocular depth estimation under challenging conditions. In *Proceedings of the IEEE/CVF international conference on computer vision*, pages 8177–8186, 2023. [2](#)
- [14] Clément Godard, Oisín Mac Aodha, Michael Firman, and Gabriel J Brostow. Digging into self-supervised monocular depth estimation. In *Proceedings of the IEEE/CVF international conference on computer vision*, pages 3828–3838, 2019. [2](#)
- [15] Vladislav Golyanik, Soshi Shimada, Kiran Varanasi, and Didier Stricker. Hdm-net: Monocular non-rigid 3d reconstruction with learned deformation model. *CoRR*, abs/1803.10193, 2018. [1](#), [2](#)
- [16] Jahanzeb Hafeez, Seunghyun Lee, Soonchul Kwon, and Alaric Hamacher. Image based 3d reconstruction of texture-less objects for vr contents. *International journal of advanced smart convergence*, 6(1):9–17, 2017. [1](#), [2](#)
- [17] Tomáš Hodan, Pavel Haluza, Štěpán Obdržálek, Jiri Matas, Manolis Lourakis, and Xenophon Zabulis. T-less: An rgb-d dataset for 6d pose estimation of texture-less objects. In *2017 IEEE Winter Conference on Applications of Computer Vision (WACV)*, pages 880–888. IEEE, 2017. [2](#)
- [18] Muhammad Saif Ullah Khan, Alain Pagani, Marcus Liwicki, Didier Stricker, and Muhammad Zeshan Afzal. Three-dimensional reconstruction from a single rgb image using deep learning: A review. *Journal of Imaging*, 8(9), 2022. [2](#)
- [19] Klaas Klasing, Daniel Althoff, Dirk Wollherr, and Martin Buss. Comparison of surface normal estimation methods for range sensing applications. In *2009 IEEE international conference on robotics and automation*, pages 3206–3211. Ieee, 2009. [2](#)
- [20] Jan Eric Lenssen, Christian Osendorfer, and Jonathan Masci. Deep iterative surface normal estimation. In *Proceedings of the IEEE/CVF conference on computer vision and pattern recognition*, pages 11247–11256, 2020. [2](#)
- [21] Andreas Ley, Ronny Hänsch, and Olaf Hellwich. Reconstructing white walls: Multi-view, multi-shot 3d reconstruction of textureless surfaces. *ISPRS Annals of Photogrammetry, Remote Sensing & Spatial Information Sciences*, 3(3), 2016. [1](#), [2](#)

- [22] Xi Li and Ping Kuang. 3d-vrvt: 3d voxel reconstruction from a single image with vision transformer. In *2021 International Conference on Culture-oriented Science & Technology (ICCST)*, pages 343–348. IEEE, 2021. 1, 2
- [23] Bogdan Maxim and Sergiu Nedeveschi. A survey on the current state of the art on deep learning 3d reconstruction. In *2021 IEEE 17th International Conference on Intelligent Computer Communication and Processing (ICCP)*, pages 283–290. IEEE, 2021. 2
- [24] Yue Ming, Xuyang Meng, Chunxiao Fan, and Hui Yu. Deep learning for monocular depth estimation: A review. *Neuro-computing*, 438:14–33, 2021. 2
- [25] Paritosh Mittal, Yen-Chi Cheng, Maneesh Singh, and Shubham Tulsiani. Autosdf: Shape priors for 3d completion, reconstruction and generation. In *Proceedings of the IEEE/CVF Conference on Computer Vision and Pattern Recognition*, pages 306–315, 2022. 2
- [26] Željko Santoši, Igor Budak, Vesna Stojaković, Mario Šokac, and Dorde Vukelić. Evaluation of synthetically generated patterns for image-based 3d reconstruction of texture-less objects. *Measurement*, 147:106883, 2019. 1, 2
- [27] Zai Shi, Zhao Meng, Yiran Xing, Yunpu Ma, and Roger Wattenhofer. 3d-retr: end-to-end single and multi-view 3d reconstruction with transformers. *arXiv preprint arXiv:2110.08861*, 2021. 2
- [28] Soshi Shimada, Vladislav Golyanik, Christian Theobalt, and Didier Stricker. Ismo-gan: Adversarial learning for monocular non-rigid 3d reconstruction. *CoRR*, abs/1904.12144, 2019. 1, 2
- [29] Jaime Spencer, C Stella Qian, Chris Russell, Simon Hadfield, Erich Graf, Wendy Adams, Andrew J Schofield, James H Elder, Richard Bowden, Heng Cong, et al. The monocular depth estimation challenge. In *Proceedings of the IEEE/CVF Winter Conference on Applications of Computer Vision*, pages 623–632, 2023. 2
- [30] Chen Sun, Abhinav Shrivastava, Saurabh Singh, and Abhinav Gupta. Revisiting unreasonable effectiveness of data in deep learning era. In *Proceedings of the IEEE international conference on computer vision*, pages 843–852, 2017. 2
- [31] Xingyuan Sun, Jiajun Wu, Xiuming Zhang, Zhoutong Zhang, Chengkai Zhang, Tianfan Xue, Joshua B Tenenbaum, and William T Freeman. Pix3d: Dataset and methods for single-image 3d shape modeling. In *Proceedings of the IEEE conference on computer vision and pattern recognition*, pages 2974–2983, 2018. 2
- [32] Jiapeng Tang, Xiaoguang Han, Mingkui Tan, Xin Tong, and Kui Jia. Skeletonnet: A topology-preserving solution for learning mesh reconstruction of object surfaces from rgb images. *IEEE transactions on pattern analysis and machine intelligence*, 44(10):6454–6471, 2021. 2
- [33] Leslie Ching Ow Tiong, Dick Sigmund, and Andrew Beng Jin Teoh. 3d-c2ft: Coarse-to-fine transformer for multi-view 3d reconstruction. In *Proceedings of the Asian Conference on Computer Vision*, pages 1438–1454, 2022. 2
- [34] Aggeliki Tsoli and Antonis. A. Argyros. Patch-based reconstruction of a textureless deformable 3d surface from a single rgb image. In *Proceedings of the IEEE/CVF International Conference on Computer Vision (ICCV) Workshops*, 2019. 1, 2
- [35] Nanyang Wang, Yinda Zhang, Zhuwen Li, Yanwei Fu, Wei Liu, and Yu-Gang Jiang. Pixel2mesh: Generating 3d mesh models from single rgb images. In *Proceedings of the European conference on computer vision (ECCV)*, pages 52–67, 2018. 1, 2
- [36] Xiaolong Wang, David Fouhey, and Abhinav Gupta. Designing deep networks for surface normal estimation. In *Proceedings of the IEEE conference on computer vision and pattern recognition*, pages 539–547, 2015. 2
- [37] Xuan Wang, Mathieu Salzmann, Fei Wang, and Jizhong Zhao. Template-free 3d reconstruction of poorly-textured nonrigid surfaces. In *Computer Vision—ECCV 2016: 14th European Conference, Amsterdam, The Netherlands, October 11–14, 2016, Proceedings, Part VII 14*, pages 648–663. Springer, 2016. 1
- [38] Oliver Wasenmüller and Didier Stricker. Comparison of kinect v1 and v2 depth images in terms of accuracy and precision. In *Asian Conference on Computer Vision*, pages 34–45. Springer, 2016. 5
- [39] Xin Wen, Junsheng Zhou, Yu-Shen Liu, Hua Su, Zhen Dong, and Zhizhong Han. 3d shape reconstruction from 2d images with disentangled attribute flow. In *Proceedings of the IEEE/CVF conference on computer vision and pattern recognition*, pages 3803–3813, 2022. 2
- [40] Aji Resindra Widya, Yusuke Monno, Masatoshi Okutomi, Sho Suzuki, Takuji Gotoda, and Kenji Miki. Whole stomach 3d reconstruction and frame localization from monocular endoscope video. *IEEE Journal of Translational Engineering in Health and Medicine*, 7:1–10, 2019. 2
- [41] Jiajun Wu, Yifan Wang, Tianfan Xue, Xingyuan Sun, Bill Freeman, and Josh Tenenbaum. Marrnet: 3d shape reconstruction via 2.5 d sketches. *Advances in neural information processing systems*, 30, 2017. 2
- [42] Haozhe Xie, Hongxun Yao, Xiaoshuai Sun, Shangchen Zhou, and Shengping Zhang. Pix2vox: Context-aware 3d reconstruction from single and multi-view images. In *Proceedings of the IEEE/CVF international conference on computer vision*, pages 2690–2698, 2019. 2
- [43] Haozhe Xie, Hongxun Yao, Shengping Zhang, Shangchen Zhou, and Wenxiu Sun. Pix2vox++: Multi-scale context-aware 3d object reconstruction from single and multiple images. *International Journal of Computer Vision*, 128(12): 2919–2935, 2020. 2
- [44] Zhen Xing, Yijiang Chen, Zhixin Ling, Xiangdong Zhou, and Yu Xiang. Few-shot single-view 3d reconstruction with memory prior contrastive network. In *European Conference on Computer Vision*, pages 55–70. Springer, 2022. 2
- [45] Zhen Xing, Hengduo Li, Zuxuan Wu, and Yu-Gang Jiang. Semi-supervised single-view 3d reconstruction via prototype shape priors. In *European Conference on Computer Vision*, pages 535–551. Springer, 2022. 2
- [46] Xuyuan Yang and Guang Jiang. A practical 3d reconstruction method for weak texture scenes. *Remote Sensing*, 13(16): 3103, 2021. 1
- [47] Zhenpei Yang, Zhile Ren, Miguel Angel Bautista, Zaiwei Zhang, Qi Shan, and Qixing Huang. Fvor: Robust joint shape

- and pose optimization for few-view object reconstruction. In *Proceedings of the IEEE/CVF Conference on Computer Vision and Pattern Recognition*, pages 2497–2507, 2022. [2](#)
- [48] Botao Ye, Sifei Liu, Xueting Li, and Ming-Hsuan Yang. Self-supervised super-plane for neural 3d reconstruction. In *Proceedings of the IEEE/CVF Conference on Computer Vision and Pattern Recognition*, pages 21415–21424, 2023. [2](#)
- [49] Yi Yuan, Jilin Tang, and Zhengxia Zou. Vanet: a view attention guided network for 3d reconstruction from single and multi-view images. In *2021 IEEE International Conference on Multimedia and Expo (ICME)*, pages 1–6, 2021. [2](#)
- [50] Anny Yuniarti and Nanik Suciati. A review of deep learning techniques for 3d reconstruction of 2d images. In *2019 12th International Conference on Information & Communication Technology and System (ICTS)*, pages 327–331. IEEE, 2019. [2](#)
- [51] Biao Zhang and Peter Wonka. Training data generating networks: Shape reconstruction via bi-level optimization. *arXiv preprint arXiv:2010.08276*, 2020. [2](#)